





35 **1 Introduction**

36 Solar eclipse provides opportunity to study the causes of drastic changes in the atmosphere arising from  
37 reduction in solar radiation and plasma flux. The atmosphere responded to this changes by modifying the  
38 electrodynamic processes and ionization supply of its species to the nighttime-like characteristics during  
39 the daytime. Different physical mechanisms (e.g. neutral wind, thermospheric composition, diffusion  
40 process etc.) that explain the distribution of plasma at the different ionospheric layers are well established.  
41 However, these mechanisms do compete with themselves in explaining other layers, especially for the  
42 topmost F2 layers (see Gulyaeva, 2011).

43

44 At mid-latitudes, the effect of diffusion processes and its relationship with the thermospheric compositions  
45 has been extensively studied during episodes of solar eclipse (Muller-Wodarg et al., 1998; Jakowski et al.,  
46 2008; Le et al., 2009; Wang et al., 2010; Chuo, 2013). However, at equatorial and low-latitude regions, the  $E$   
47  $\times B$  plasma drift had been used to explain the circumstances of solar eclipse on transport processes (Adeniyi  
48 et al., 2007; Adekoya et al., 2015). Recently, attention has been drawn to the study of the topmost  
49 ionosphere during an eclipse for improved prediction and modelling (Huba and Drob, 2017; Chnriak and  
50 Zakharenkova, 2018). Reinisch et al., (2018) compared the modelled and measured studies of electron  
51 densities at the altitude range of about 150 - 400 km during the eclipse. They found that at lower altitude  
52 (at about 150 km) the modelled and the measured agreed well to the changes in the altitude profile of  
53 electron density compared to at higher altitudes. The authors however posited that it would be improved if  
54 the model NmF2 peak falls more slowly to better match the data. Consequently, the present study  
55 investigates the effects of solar eclipse of August 21, 2017 on the constituents of the ionosphere at mid-  
56 latitudes. This, we intend to achieve by analysing the ionospheric parameters that controls the distribution  
57 of plasma at the topside and bottomside layers of the F2 region. To shed light on these analysis, section 2  
58 highlights the data source, methodology, and path of the eclipse. The result and discussion was presented  
59 in section 3. Section 4 presented the summary and concluding remark of the result.

60

61 **2 Data source, methodology, and the path of the eclipse**

62 With regards to the eclipse of 21 August 2017, the totality of the eclipse is visible from within a narrow  
63 corridor that traverses the United States of America. However, in the surrounding areas, which include all  
64 of mainland United States and Canada, the eclipse was partial. More details of its path can be seen via  
65 NASA – Total solar eclipse of 2017 August 21 (<https://eclipse.gsfc.nasa.gov/>). From the footprint of the  
66 Moon's shadow as seen from some locations, the eclipse started from around 08:00 LT and ended around  
67 14:30 LT (not shown). The details on the local circumstances of the eclipse, the time of the first, mid and  
68 last contact of the eclipse over the ionosphere of the investigated stations were highlighted in table 1.



69 More details on the total solar eclipse event and its partiality, the circumstances surrounding its  
70 progression and its magnitude of obscuration can be obtained through the link  
71 [http://xjubier.free.fr/en/index\\_en.html](http://xjubier.free.fr/en/index_en.html). The ionospheric parameters data used for this study for the  
72 selected mid-latitude stations were obtained from the Global Ionospheric Radio Observatory (GIRO)  
73 networks (Reinisch and Galkin 2011) and manually validated. The parameters include the critical frequency  
74 of the F2-layer ( $f_oF2$ , Hz), and its height ( $h_mF2$ , km), the shape parameter (B1), the thickness parameter  
75 (B0), and the Chapman scale height (H) of the F2 layer. The path of the eclipse informed the choice of  
76 stations.

77  $NmF2$  values for both the eclipse and control days were obtained from their corresponding critical  
78 frequencies ( $f_oF2$ ) using the expression:  $NmF2 = ((f_oF2)^2 / 80.5) \text{ e/m}^3$ . The control day value is the mean of  
79 the values obtained on respective days that have similar geomagnetic properties with the eclipse day, but  
80 without eclipse. The typical behaviour of the  $NmF2$  and  $h_mF2$  on the eclipse day (i.e.  $NmF2e$  and  $h_mF2e$ )  
81 was compared with that of the control day ( $NmF2c$  and  $h_mF2c$ ) to observe the changes brought by the  
82 short period of loss of photoionization in the ionosphere. This will measure the direct consequence of the  
83 solar radiation disruption (due to the eclipse) on the ionospheric chemical, transport and thermal processes  
84 in the F2 layer. The ionized layer depends majorly on three parameters, viz:  $NmF2$ ,  $h_mF2$ , and the  
85 ionospheric scale height (H). The H describes the constituents of the ionospheric plasma, which decreases  
86 with increasing altitude. It is estimated from the fitted  $\alpha$ -Chapman layer with a variable scale height,  $H(h)$ ,  
87 to the measured bottomside profile  $N(h)$ , which then determined as the Chapman scale height at  $h_mF2$  (i.e.  
88  $H(h_mF2) = H$ ) (Huang and Reinisch 2001; Reinisch and Huang 2001). Together with the information of  $NmF2$   
89 and  $h_mF2$ , the topside profile can be best represented, which is assumed to follow the  $\alpha$ -Chapman function  
90 (Huang and Reinisch 2001). Also, H provides a linkage between the bottomside ionosphere and the topside  
91 profiles of the F layer (Liu et al., 2007).

92

93 However, Xu et al. (2013) and Gulyaeva (2011) related ionospheric F2 layer scale height, H to the topside  
94 base scale height,  $H_{sc}$ , given by  $H_{sc} = h_{sc} - h_mF2 \approx 3 \times H$ . Where  $h_{sc}$  is the height at which the electron  
95 density of the F2-layer falls by a factor of an exponent, at an upper limit of 400 km altitude (i.e.  $NmF2/e$ )  
96 (see Xu et al., 2013). That is, the region where electron density profile gradient is relatively low. Gulyaeva  
97 (2011) showed theoretically that  $H_{sc}$  increase over  $H_m$  by a factor of approximately three (3) and is a  
98 consequence of the  $Ne/NmF2$  ratio ( $Ne$  – plasma density), which corresponds to H in the Chapman layer. At  
99 altitudes very close to  $h_mF2$ , the ratio equals 0.832, while it is 0.368 at altitudes beyond the  $h_mF2$ .  
100 Therefore, we adopted the definition of Gulyaeva (2011) for the topside base scale height as the region of  
101 the ionosphere between the F2-peak and 400 km altitude. Summarily, the topside based scale height



102 ionosphere here is defined as the region between the F2 peak and hsc or 3H. It is thus evident that H is a  
103 key and essential parameter in the continuity equation for deriving the production rate at different  
104 altitudes, a pointer to the F2 topside electron profiler, as well as a good parameter for evaluating the  
105 transport term (Yonezawa, 1966; Huang and Reinisch, 2001; Reinisch and Huang, 2001; Belehaki et al.,  
106 2006; Reinisch et al., 2004). Consequently, the parameter H can be used as a proxy for observation relating  
107 to the topmost side electron density profile. Furthermore, the division of the topsides and the bottomside  
108 ionosphere may be related to the difference in the effective physical mechanisms in the regions. Hence, the  
109 bottomside parameters B1 and B0 of the ionosphere, as presented in this work, helped in examining the  
110 perturbation of solar eclipse in the bottomside ionospheric F2 layer.

111

### 112 **3 Result and Discussion**

113 This section presents the temporal evolution of the maximum electron density ( $NmF2$ ), and its  
114 corresponding height ( $hmF2$ ) over the ionosphere at the selected mid-latitude stations along the path of  
115 solar eclipse of 21 August 2017. The control day variation relative to the eclipse day is also presented.  
116 Figure 1 presents the variation of maximum electron density and the corresponding peak height, during  
117 both the eclipse and control days. Figure 2 depicts the variation of scale height and the bottomside  
118 parameters (B0 and B1) due to the eclipse by superposing plots for both the eclipse and control days.  
119 Analysis of these parameters during an eclipse event may help in the modelling of the ionospheric profiles  
120 (the topsides and bottomside electron density distribution profile) during the short nighttime-like period of  
121 the day. Figure 1a presents the  $NmF2$  and  $hmF2$  variations during the eclipse event and the control day  
122 over Austin; having an obscuration magnitude of 65.93% around the daytime period. The effect of the  
123 disruption of solar radiation was evident as the  $NmF2$  started decreasing at the first contact of the eclipse  
124 in Fig. 1ai. The start time or first contact, the maximum magnitude period and the end time or the last  
125 contact of the eclipse are marked with the vertical lines S, M and E respectively. The decrement in  $NmF2$   
126 during the eclipse phase was due to reduction in the ionization. This reduction caused changes in the  
127 photochemical and transport process of the atmosphere during the daytime, thus exhibiting nighttime  
128 characteristics. It should be noted that the maximum decrease in  $NmF2$  did not coincide with the maximum  
129 magnitude of the eclipse obscuration, rather with a time lag of few minutes. This lag period fell within the  
130 relaxation period over Austin ionosphere, with  $NmF2$  and  $hmF2$  simultaneously attaining their peak  
131 magnitudes. Hence, the ionosphere returned to its pre-eclipse state. Contrary to the decrease in the  $NmF2$   
132 amplitude, the  $hmF2$  increased at the total obscuration of the eclipse window.

133

134 The ionosphere over Eglin AFB, Boulder, Point Arguello, Millstone Hill and Idaho National Lab, did not show  
135 any contrary variation to that observed at Austin during the eclipse event. The decrease and increase in



136 NmF2 and hmF2 after the maximum magnitude was simultaneous. The only exception was that the local  
137 time at which each station observed the effects were different. Their obscuration percentage ranged from  
138 62.5 – 100%. This did not cause any significant change in the way they responded to the reduction in solar  
139 heating. The ionosphere over Idaho National Lab experienced the totality of the eclipse with 100 %  
140 magnitude, the hmF2 was observed to increase few minutes before the maximum magnitude of the  
141 obscuration. However, other stations responded differently, their hmF2 peak enhancement was observed  
142 after the maximum obscuration. All these observations may be linked with the fact that the level of  
143 minimum rate of electron production does not necessarily coincide with peak electron density of the  
144 molecular gases formed. This is because the electron concentration depends on the loss rate by dissociative  
145 recombination too.

146

147 At mid-latitudes, the ionospheric F2 plasma distribution is controlled by diffusion processes (Rishbeth  
148 1968). There are two basic mechanisms that define the diffusion process during an eclipse: First is the  
149 coolness brought by the partial removal of photoionization (Müller-Wodarg et al., 1998), which is believed  
150 to be the originator of the downward diffusion process, and the atmospheric expansion due to the gradual  
151 increase in the temperature after the totality. The downward diffusion process was related to the increase  
152 in the molecular gas (N<sub>2</sub>) concentration during the cooling process. However, the aftermath of the coolness  
153 was related to the upward diffusion process. These mechanisms were proxy to the electron density  
154 distribution during the eclipse window. Our analysis suggests that the observed decrease in NmF2 is due to  
155 the downward diffusion flux of the plasma while the increase that followed is by upward diffusion (e.g. Le  
156 et al., 2009; Adekoya and Chukwuma 2016). Several works on eclipse (Müller-Wodarg et al., 1998;  
157 Grigorenko et al., 2008; Adekoya and Chukwuma 2016; Hoque et al., 2016) have shown that it was not just  
158 the electron density that is being affected during an eclipse window, but the thermospheric wind as well,  
159 since the thermospheric wind emanating from the ratio of gas species is related to the variation in electron  
160 density. It has been observed that the increase in the mean molecular gas of thermospheric composition  
161 decreases the electron density and vice versa. Le et al. (2010) related the trough of electron density  
162 distribution during the eclipse phases to the contraction/compression and expansion of the atmosphere  
163 brought by the decrease and increase in temperature; leading to the downward drift of the plasma during  
164 the eclipse window. Chukwuma and Adekoya (2016) attributed the decrease in the electron temperature to  
165 the downward vertical transport process and the decrease in the cooling process to the upward vertical  
166 transport process.

167

168 Figure 2 describes H, B1 and B0 in three columns respectively for all six stations. It was observed from the  
169 plots that the minimum decrease in NmF2 amplitude corresponds to increase in H at all stations; implying



170 the upward lifting of the topside electron to the region of higher altitude at the eclipse window. Hence, the  
171 scale height variation highlights the decrease in electron production and the vertical distance through  
172 which the pressure gradient falls at the topside during the eclipse activity. The observation illustrates the  
173 mutual relationship between the NmF2 and H, which may aid in extrapolating the topside ionospheric  
174 profile (Gulyaeva, 2011). In essence, scale height changes observed during the eclipse window can be used  
175 to explain the pressure gradient, electron density distribution and transport processes. In this sense, the  
176 diffusion coefficients are expressed as ratio of determinants (determinant here refers to the concentration  
177 of species ([O] and [N<sub>2</sub>]), with the size of the determinants depending upon both the number of species in  
178 the gas mixture and the level of approximation. Therefore, the increase (decrease) in the scale height can  
179 be used as a proxy for downward (upward) diffusion process at the topside ionosphere. Consequently, the  
180 thermospheric wind, which causes plasma distribution in the topside ionosphere, is induced by solar  
181 radiation. Moreover, the significant changes observed in the scale height variation during the eclipse  
182 window also indicated that transport processes are affected as they are temperature dependent.  
183 Therefore, changes in the thermospheric compositions due to the solar eclipse at the topside layer will  
184 affect the density profiles of the ionosphere (Müller-Wodarg et al., 1998).

185

186 It is noteworthy that the increase (decrease) in the scale height decreases (increases) the electron density  
187 during the eclipse window. The sensitivity of electron density to temperature at the topside directly affects  
188 the electron density profile (e.g. Wang et al., 2010); as cooling due to decrease in temperature results in  
189 decrease in the electron density via reduced ionization. This indicates that the decrease (increase) in  
190 electron temperature at the topside ionosphere causes the increase (decrease) in the scale height, which is  
191 related to the diffusion and transport processes and subsequently affect the pressure gradient of the  
192 plasma. From plots of H (fig. 2) and NmF2 (fig. 1), it was observed that the minimum decrease in NmF2  
193 corresponded with peak increase in scale height. This imply that the topside ionosphere is more sensitive  
194 (than the bottomside) to any change in the solar radiation. Thus, the pressure gradients can be analysed in  
195 terms of either the scale height or electron density.

196

197 From column 2 and 3 of Figure 2, we observed that the measured shape (B1) and thickness (B0) parameters  
198 of the ionosphere over these stations exhibit significant variations during the eclipse event. B1 responded  
199 with a decrease at the first contact of the eclipse compared to the control day. This behaviour differs from  
200 that of the B0 observation. B0 parameter from the first contact increases and reached the maximum peak  
201 few minutes after the maximum obscuration magnitude, which coincided with the minimum decrease in  
202 B0. Generally, the pattern of the day to day variation of the bottomside parameters is the average  
203 morphology, but the increase in the B0 and the decrease in the B1 parameters during the eclipse period



204 compared to the control day was a notable one and can be related to the perturbation caused by the solar  
205 eclipse. During the eclipse, the solar radiation was lost; trapped atomic ions  $O^+$  was converted into  
206 molecular ion ( $NO^+$  and  $O_2^+$ ) by charge transfer, owing to the sufficient concentration of molecular gasses  
207 ( $N_2$  and  $O_2$ ) (Rishbeth, 1988). The height of the ionospheric slab indeed increased with reduced width,  
208 which is attributable to compression due to loss of solar heating.

209 The behaviour of the ionosphere can be explained during solar eclipse with any of the components that  
210 constitute the topside and the bottomside ionosphere and can be looked at, from the angle of the  
211 percentage concentration of the components. In this regard, the percentage deviations of NmF2 (DNmF2)  
212 and hmF2 (DhmF2) during the eclipse day away from the control day were plotted in figure 3. This is done  
213 to describe the contribution of the thermospheric wind and compositions. The percentage deviation was  
214 defined as the ratio of  $(NmF2e - NmF2c)/NmF2c \times 100$ . The same relation is defined for the hmF2  
215 parameter. As earlier pointed out, during eclipse period, neutral composition becomes the dominant  
216 chemical process arising from diffusion activities. The increase in the neutral composition leads to the  
217 increase in the molecular gas concentration and compete with diffusion process. Hence the percentage  
218 deviation in Fig. 3 discusses the neutral composition changes and delineate how these changes may affect  
219 the electron densities as well as its profiles in the atmosphere during the eclipse. The respective maximum  
220 and minimum peak response of the percentage deviation is attributed to the enhancement and depletion  
221 of DNmF2. One sees from the plots that the percentage deviation started increasing at the first contact of  
222 the eclipse (the dash vertical line) and reached the maximum, appearing few minutes after the maximum  
223 magnitude of the eclipse was obtained. This behaviour is similar to the conditions of the neutral  
224 compositions during the eclipse event reported by Muller-Wodarg et al. (1998).

225

226 Another important process observed in this study is the neutral wind flow effect. The decrease in the  
227 electron density during the first phase of the eclipse, and due to the decrease in temperature was trailed to  
228 the increase in the percentage deviation. During this process, the neutral wind flow in the westward  
229 direction, and then returned eastward during the recovery phase of the eclipse. The increase/decrease in  
230 the DNmF2 observation was attributed to the westward and eastward flow of the neutral wind. The  
231 intensity of this deviation responds directly to the rate of flow of the neutral species brought by loss in  
232 photoionization. Thus, the changes in the percentage deviation observed during the eclipse window in the  
233 present study were the consequence of the neutral wind response. The plot in Figure 3 had established the  
234 ionospheric dynamics of diffusion processes, neutral compositions and the flow of neutral wind caused by  
235 the eclipse perturbation, which can invariably reduce the effectiveness and reliability of radio wave  
236 propagation.

237



238 Relative to the mutual relationship between the topside and bottomside ionosphere, we considered the  
239 linear correlation coefficient ( $R$ ) of  $H$  versus  $hmF2$  and  $H$  versus  $B0$  during the eclipse window, Figure 4.  $R$   
240 ranges from (0.52-0.92) for  $H/hmF2$  relationship, and 0.37-0.92 for the  $H/B0$  connection. This good linear  
241 agreement revealed the dependence of  $hmF2$  and  $B0$  on the scale height. The only exception where low  
242 correlation was observed was at Millstone (0.37) with respect to the  $H$  versus  $B0$  relationship. Apart from  
243 revealing the dependence between the parameters, the relationship may also provide a convenient way for  
244 modelling the topside profile from the knowledge of the bottomside parameter,  $B0$ , during the eclipse  
245 period. Also, the strong correlation between  $hmF2$  and  $H$  indicates that there may be some inter-related  
246 physical mechanisms controlling the behaviour of the plasma at the topside ionosphere. That is  $hmF2$   
247 strongly depend on the neutral wind flow and explain the state of thermospheric composition (Liu et al.,  
248 2006; Fisher et al., 2015). Since all these parameters competes during the eclipse, one can argue that with  
249 the accessibility of one, in place of the other (as a consequence of their relationship), the prediction and  
250 modelling of the ionosphere can be conveniently achieved.

251

252 Although, the maximum magnitude of eclipse ever registered is not more than 7 minutes, its period of  
253 progression, from first contact to the last contact, sometimes can be prolonged for more than 3 hours. This  
254 period is enough for persistence of perturbation of the ionospheric processes to affect the radio  
255 propagation. The International Reference Ionosphere model (IRI-model) have since made it easier for  
256 validation of any direct measurement data of the ionosphere and improving the understanding of the basic  
257 mechanism of the ionosphere. However, The IRI was modelled for both the F2 layer and the  
258 topmost/plasmasphere electron density profile of the ionosphere based on the global available data from  
259 the ground-based as well as satellite observations (Bilitza and Reinisch, 2008). It has however been  
260 continually upgraded with new experimental data and modelling approach, which resulted in the improved  
261 version (Bilitza and Reinisch 2008; Bilitza et al., 2014; 2017). However, with the improved version that  
262 considered both the plasmaspheric and the F2 layer topside and bottomside electron density profiles, the  
263 IRI model does not capture the conditions of the ionosphere during solar eclipse. This we assumed may be  
264 due to the time resolution (IRI model predictions have a nominal time resolution of 4 hours) that was  
265 considered in the capturing of the IRI parameters. Therefore, the need to capture the ionospheric  
266 perturbation emanating from the action of solar eclipse in the modelling efforts of the IRI Committee by  
267 considering higher time resolution.

268

269

270





271 **4 Conclusions**

272 This paper presents the induced perturbation of solar eclipse of 21 August 2017 on the ionospheric F  
273 parameters and their behaviour in predicting one another at mid-latitude. The perturbation effects and  
274 dynamics during a solar eclipse episode using ionospheric F2 parameters (NmF2 and hmF2), the bottomside  
275 profile thickness (B0) and shape (B1) parameters of electron density and the plasma scale height (H), which  
276 are not often used for eclipse study, were investigated. These parameters represent the state of the F layer  
277 ionosphere. The changes observed during the eclipse phase is related to the reduction in solar radiation  
278 and natural gas heating. The NmF2 minimum was attained at ~30 minutes after the totality of the eclipse  
279 when it decreases to about 65% of its control day. This decrease in NmF2 was uplifted to the higher altitude  
280 compared to the non-eclipse day. The thickness and shape parameters which are often limited to the  
281 bottomside F-layer were seen as viable parameters for probing the topside ionosphere, relative to the scale  
282 height during the eclipse. Hence their relationship in predicting one another is established. Implication is  
283 that eclipse-caused perturbation could have been better explained using some ionosonde parameters. The  
284 changes in the neutral wind flow, thermospheric compositions and diffusion processes found their  
285 explanation in the behaviour of the F layer plasma during the eclipse. Therefore, the need for IRI model  
286 developers to capture eclipse-related perturbations in the IRI model development by considering higher  
287 time resolution.

288

289 **Acknowledgements**

290 We acknowledge use of global ionospheric Radio Observatory data provided by ULMCAR  
291 (<http://ulcar.uml.edu/DIDBase/>) and the World Data Center for Geomagnetism, Kyoto  
292 (<http://wdc.kugi.kyoto-u.ac.jp/index.html>) for geomagnetic activity data. We thank the management team  
293 of the national Aeronautics and Space Administration (NASA) service (<http://eclipse.gsfc.nasa.gov>) and  
294 [http://xjubier.free.fr/en/site\\_pages/SolarEclipseCalc\\_Diagram.html](http://xjubier.free.fr/en/site_pages/SolarEclipseCalc_Diagram.html) for progression and eclipse local  
295 circumstances information.

296

297

298

299

299 **References**

300 Adeniyi, J. O., Radicella, S. M., Adimula, I. A., Willoughby, A. A., Oladipo, O. A., and Olawepo, O.: Signature  
301 of the 29 March 2006 eclipse on the ionosphere over an equatorial station, *J. Geophys. Res.*, 112 (A6),  
302 A06314. <http://dx.doi.org/10.1029/2006JA012197>, 2007.

303

304 Adekoya, B. J., Chukwuma, V. U., and Reinisch, B. W.: Ionospheric vertical plasma drift and electron density  
305 response during total solar eclipses at equatorial/low latitude, *J. Geophys. Res.*, 120, 8066-8084.  
306 doi:10.1002/2015JA021557, 2015.

307

308 Adekoya, B. J., and Chukwuma, V. U.: Ionospheric F2 layer responses to total solar eclipses at low- and mid-  
309 latitude, *J. Atmos. Sol. Terr. Phys.*, 138-139, 136-160. <http://dx.doi.org/10.1016/j.jastp.2016.01.006>, 2016.

310



- 311 Belehaki, A., Marinov, P., Kutiev, I., Jakowski, N., and Stankov, S.: Comparison of the topside ionosphere  
312 scale height determined by topside sounders model and bottomside digisonde profiles, *Adv. Space Res.*,  
313 <http://dx.doi.org/10.1016/j.asr.2005.09.015>, 2006.  
314
- 315 Bilitza, D. and Reinisch, B. W.: International Reference Ionosphere 2007: improvements and new  
316 parameters, *Adv. Space Res.* 42, 599-609. <http://dx.doi.org/10.1016/j.asr.2007.07.048> , 2008.  
317
- 318 Bilitza, D., Altadill, D., Zhang, Y., Mertens, C., Truhlik, V., Richards, P., McKinnell, L. -A., and Reinisch, B.: The  
319 International Reference Ionosphere 2012 - A model of international collaboration, *J. Space Weather Space  
320 Clim.*, 4, 1-12. doi:10.1051/swsc/2014004, 2014.  
321
- 322 Bilitza, D., Altadill, D., Truhlik, V., Shubin, V., Galkin, I., Reinisch, B., and Huang, X.: International Reference  
323 Ionosphere 2016: From ionospheric climate to real-time weather predictions, *Space Weather*, 15, 418-429.  
324 <http://dx.doi.org/10.1002/2016SW001593> , 2017.  
325
- 326 Cherniak, I., and Zakharenkova, I.: Ionospheric Total Electron Content response to the great American solar  
327 eclipse of 21 August 2017, *Geophys. Res. Lett.*, <http://dx.doi.org/10.1002/2017GL075989> , 2018.  
328
- 329 Chukwuma, V. U., and Adekoya, B. J.: The effects of March 20, 2015 solar eclipse on the F2 layer in the mid-  
330 latitude, *Advances in Space Research*, 58, 1720-1731. <http://dx.doi.org/10.1016/j.asr.2016.06.038> , 2016.  
331
- 332 Chuo, Y. J.: Ionospheric effects on the F region during the sunrise for the annular solar eclipse over Taiwan  
333 on 21 May 2012, *Ann. Geophys.*, 31, 1891-1898. doi:10.5194/angeo-31-1891-2013, 2013  
334
- 335 Fisher, D. J., Makela, J. J., Meriwether, J. W., Buriti, R. A., Benkhaldoun, Z., Kaab, M., and Lagheryeb, A.:  
336 Climatologies of nighttime thermospheric winds and temperatures from Fabry-Perot interferometer  
337 measurements: From solar minimum to solar maximum, *J. Geophys. Res.*, 120, 6679-6693,  
338 doi:10.1002/2015JA021170, 2015.  
339
- 340 Grigorenko, E. I., Lyashenko, M. V., and Chernogor, L. F.: Effects of the solar eclipse of March 29, 2006, in  
341 the ionosphere and atmosphere, *Geomagnetism and Aeronomy*, 48 (3), 337-351.  
342 <http://dx.doi.org/10.1134/S0016793208030092>, 2008.  
343
- 344 Gulyaeva T. L.: Storm time behaviour of topside scale height inferred from the ionosphere-plasmasphere  
345 model driven by the F2 layer peak and GPS-TEC observation, *Adv. Space Res.*, 47, 913-920.  
346 doi:10.1016/j.asr.2010.10.025, 2011.  
347
- 348 Hoque, M. M., Wenze, I. D., Jakowski, N., Gerzen, T., Berdermann, J., Wilken, V., Kriegel, M., Sato, H.,  
349 Borries, C., and Minkwitz, D.: Ionospheric response over Europe during the solar eclipse of March 20, 2015,  
350 *J. Space Weather Space Clim.*, 6 (A36). doi: 10.1051/swsc/2016032, 2016.  
351
- 352 Huba, J. D., and Drob, D.: SAMI3 prediction of the impact of the 21 August 2017 total solar eclipse on the  
353 ionosphere/plasmasphere system, *Geophys. Res. Lett.*, 44, 5928-5935.  
354 <http://dx.doi.org/10.1002/2017GL073549>, 2017.  
355
- 356 Huang, X. and B. W. Reinisch, B. W.: Vertical electron content from ionograms in real time, *Radio Sci.*, 36  
357 (2), 335 – 342, 2001.  
358



- 359 Jakowski, N., Stankov, S. M., Wilken, V., Borries, C., Altadill, D., Chum, J., Buresova, D., Boska, J., Sauli, P.,  
360 Hruska, F. and Cander, Lj. R.: Ionospheric behaviour over Europe during the solar eclipse of 3 October 2005,  
361 J. Atmos. Sol. Terr. Phys., 70, 836-853. <http://dx.doi.org/10.1016/j.jastp.2007.02.016>, 2008.  
362
- 363 Le, H., Liu, L., Yue, X., Wan, W., and Ning, B.: Latitudinal dependence of the ionospheric response to solar  
364 eclipse, J. Geophys. Res., 114, A07308. <http://dx.doi.org/10.1029/2009JA014072>, 2009.  
365
- 366 Le, H., Liu, L., Libo, D., Ding, F., Ren, Z., Zhipeng, C., Yiding, W., Weixing, N., Baiqi, G., Guirong, X., Wang,  
367 Min, L., Guozhu, X., Bo, L., Lianhuan, H.: Observations and modeling of the ionospheric behaviors over the  
368 east Asia zone during the 22 July 2009 solar eclipse. J. Geophys. Res., 115, A10313.  
369 <http://dx.doi.org/10.1029/2010JA015609>, 2010.  
370
- 371 Liu, L., Wan, W., and Ning B.: A study of the ionogram derived effective scale height around the ionospheric  
372 hmF2, Ann. Geophys., 24 (3), 851-860. [www.ann-geophys.net/24/851/2006/](http://www.ann-geophys.net/24/851/2006/), 2006.  
373
- 374 Liu, L., Le, H., Wan, W., Sulzer, M. P., Lei, J., and Zhang, M. -L.: An analysis of the scale heights in the lower  
375 topside ionosphere based on the Arecibo incoherent scatter radar measurements, J. Geophys. Res., 112,  
376 A06307, <http://dx.doi.org/10.1029/2007JA012250>, 2007.  
377
- 378 Müller-Wodarg, I. C. F., Aylward, A. D., and Lockwood, M.: Effects of a Mid-Latitude Solar Eclipse on the  
379 Thermosphere and Ionosphere - A Modelling Study, Geophys. Res. Lett., 25(20), 3787-3790, 1998.  
380
- 381 Reinisch, B. W., Dandenault, P. B., Galkin, I. A., Hamel, R., and Richards R. P.: Investigation of the electron  
382 density variation during the August 21, 2017 Solar Eclipse, Geophys. Res. Lett., doi:  
383 10.1002/2017GL076572, 2018.  
384
- 385 Reinisch, B. W. and Galkin, I. A.: Global Ionosphere Radio Observatory (GIRO), Earth Planets Space, 63 (4),  
386 377-381. <https://doi.org/10.5047/eps.2011.03.001>, 2011.  
387
- 388 Reinisch, B. W., Huang, X., Belehaki, A., Shi, J., Zhang, M., and Ilma, R.: Modeling the IRI topside profile  
389 using scale heights from ground-based ionosonde measurements, Adv. Space Res., 34 (9), 2026-2031.  
390 <https://doi.org/10.1016/j.asr.2004.06.012>, 2004.  
391
- 392 Reinisch, B. W., and Huang, X.: Deducing topside profiles and total electron content from bottomside  
393 ionograms, Adv. Space Res., 27 (1), 23-30. [https://doi.org/10.1016/S0273-1177\(00\)00136-8](https://doi.org/10.1016/S0273-1177(00)00136-8), 2001.  
394
- 395 Rishbeth, H.: Solar eclipses and ionospheric theory. Space Science Review, 8 (4), 543-554.  
396 <https://doi.org/10.1007/BF00175006>, 1968.  
397
- 398 Rishbeth, H.: Basic physics of the ionosphere: A tutorial review, Journal of Institute of The Electronics and  
399 Radio Engineers, 58 (6S), S207-S223. doi:10.1049/jiere.1988.0060, 1988.  
400
- 401 Xu, T. L., Jin, H. L., Xu, X., Guo, P., Wang, Y. B., Ping, J. S.: Statistical analysis of the ionospheric topside scale  
402 height based on COSMIC RO measurements, J. Atmos. Sol. Terr. Phys., 104, 29 – 38.  
403 <http://dx.doi.org/10.1016/j.jastp.2013.07.012>, 2013.  
404
- 405 Wang, X., Berthelier, J. J., and Lebreton, J. P.: Ionosphere variations at 700 km altitude observed by the  
406 DEMETER satellite during the 29 March 2006 solar eclipse, J. Geophys. Res., 115, A11312.  
407 <http://dx.doi.org/10.1029/2010JA015497>, 2010.  
408



409 Yonezawa, T.: Theory of formation of the ionosphere, Space Science Review, 5 (1), 3-56.  
410 <https://doi.org/10.1007/BF00179214>, 1966

411

412

413

414 **Table Caption**

415 **Table 1:** List of ionosonde station, geographic coordinate, eclipse progression time and percentage of  
416 maximum obscuration.

417

418 **Figure Captions**

419 **Figure 1:** Ionospheric NmF2 and hmF2 variations during the eclipse day (black continuous line) and the  
420 control day (dash blue line). The three vertical lines represents the different phases of the eclipse (S - start  
421 time of the initial phase, M - the period of the maximum magnitude of the eclipse, and E - the end time of  
422 the recovery phase or the last contact of the eclipse progression).

423 **Figure 2:** The local time variation of the ionospheric scale height and the bottomside (B0 and B1). The other  
424 features are the same as in Fig. 1.

425 **Figure 3:** Percentage deviation of NmF2 (DNmF2) and hmF2 (DhmF2) magnitudes during the 21 August  
426 2017 eclipse phase.

427 **Figure 4:** Linear relationship of H versus hmF2 and H versus B0 during the eclipse of 21 August 2017  
428 progression phase.

429

430

431

432

433

434

435

436

437

438

439

440

441

442

443

444

445

446

447



448 **Table 1:** List of ionosonde station, geographic coordinate, eclipse progression time and percentage of  
449 maximum obscuration.

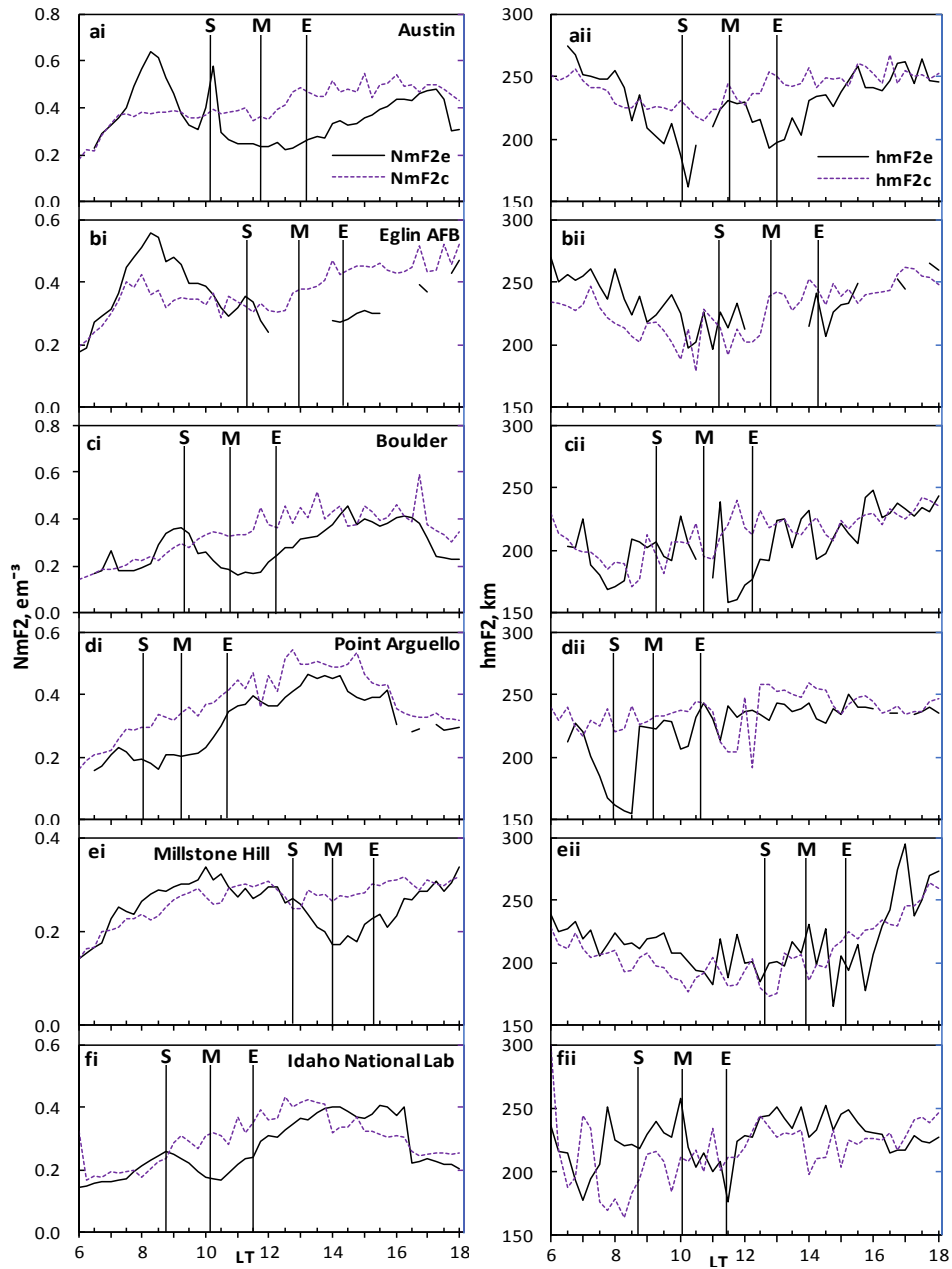
Station	GLat	GLong	Eclipse Start time (UT)	Eclipse Max Time (UT)	Eclipse End Time (UT)	% of max obscuration	UT to LT difference
AUSTIN	30.4	262.3	16:40:45.1	18:10:10.3	19:39:35.0	65.93	17:29.2
EGLIN AFB POINT	30.5	273.5	17:04:41.1	18:37:07.6	20:03:47.7	83.322	18:13.8
ARGUELLO	34.8	239.5	16:02:38.5	17:16:54.8	18:39:36.0	64.608	15:57.6
BOULDER	40	254.7	16:22:33.1	17:46:09.6	19:13:45.9	93.37	16:58.8
MILLSTONE HILL	42.6	288.5	17:27:28.1	18:45:52.5	19:58:38.3	62.533	19:13.8
IDAHO NATIONAL LAB	43.81	247.32	16:14:15.2	17:32:36.5	18:56:30.1	100	16:29.3

450

451

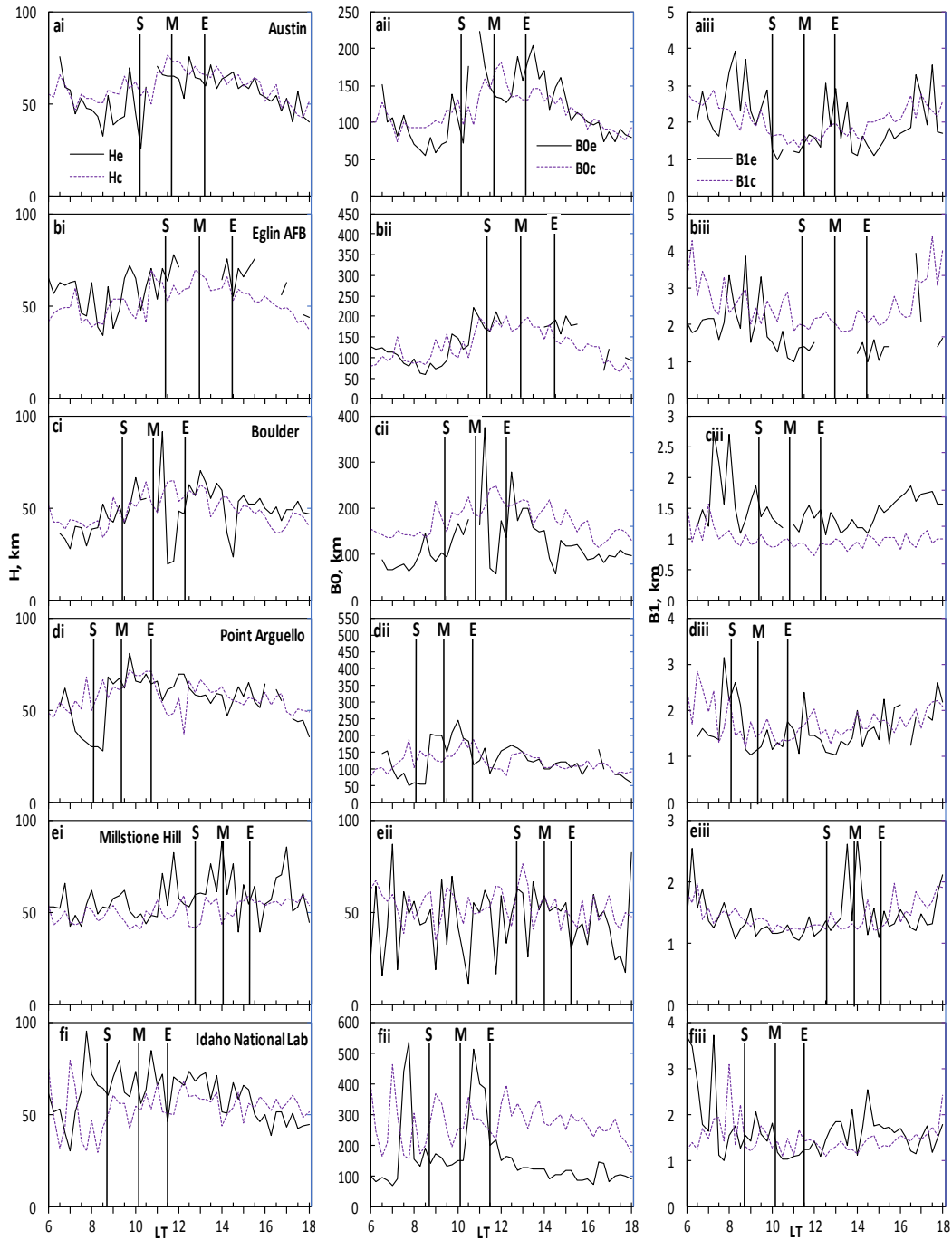
452

453



454

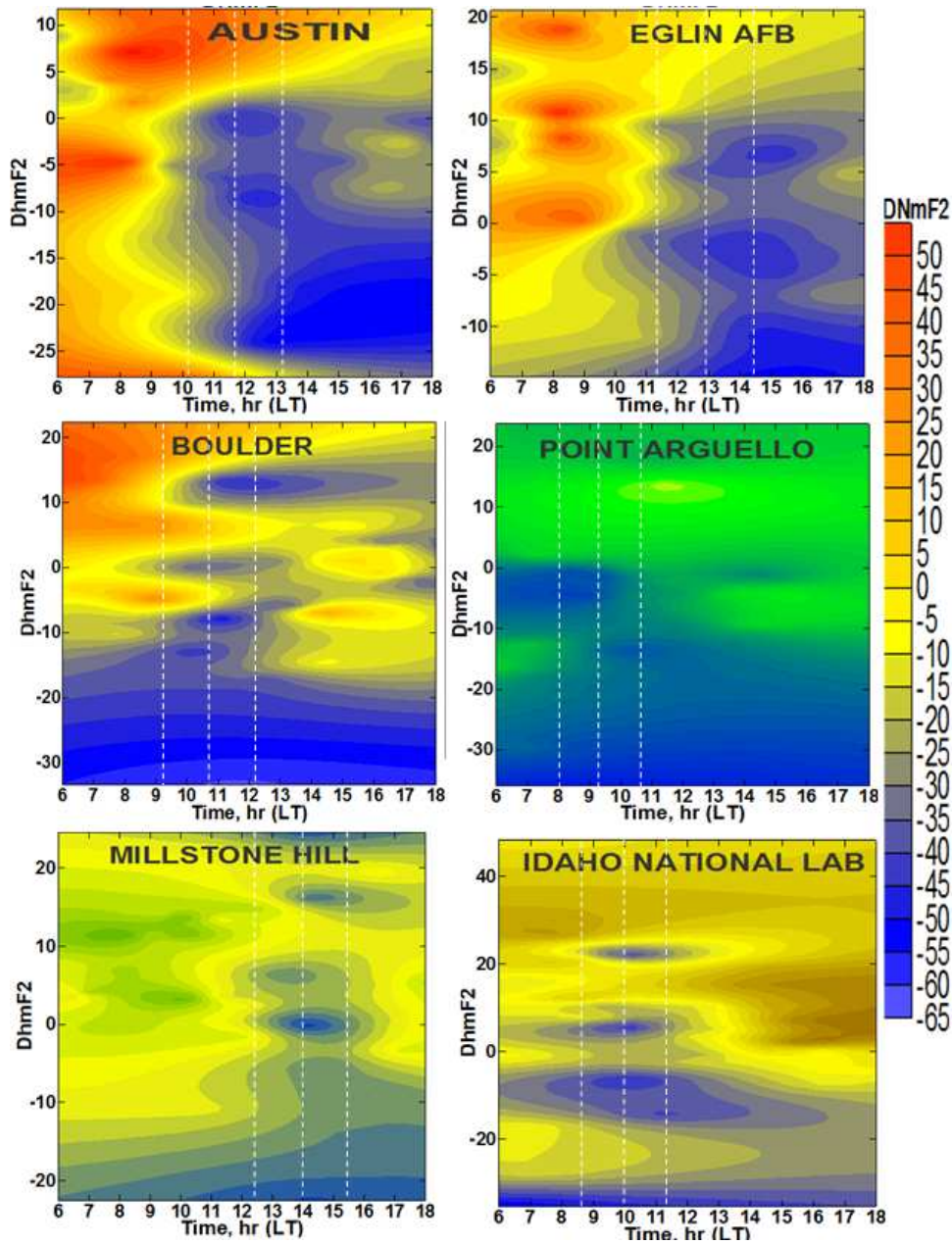
455 **Figure 1:** Ionospheric NmF2 and hmF2 variations during the eclipse day (black continuous line) and the  
 456 control day (dash blue line). The three vertical lines represents the different phases of the eclipse (S - start  
 457 time of the initial phase, M - the period of the maximum magnitude of the eclipse, and E - the end time of  
 458 the recovery phase or the last contact of the eclipse progression).



459

460 **Figure 2:** The local time variation of the ionospheric scale height and the bottomside (B0 and B1). The other  
 461 features are the same as in Fig. 1.





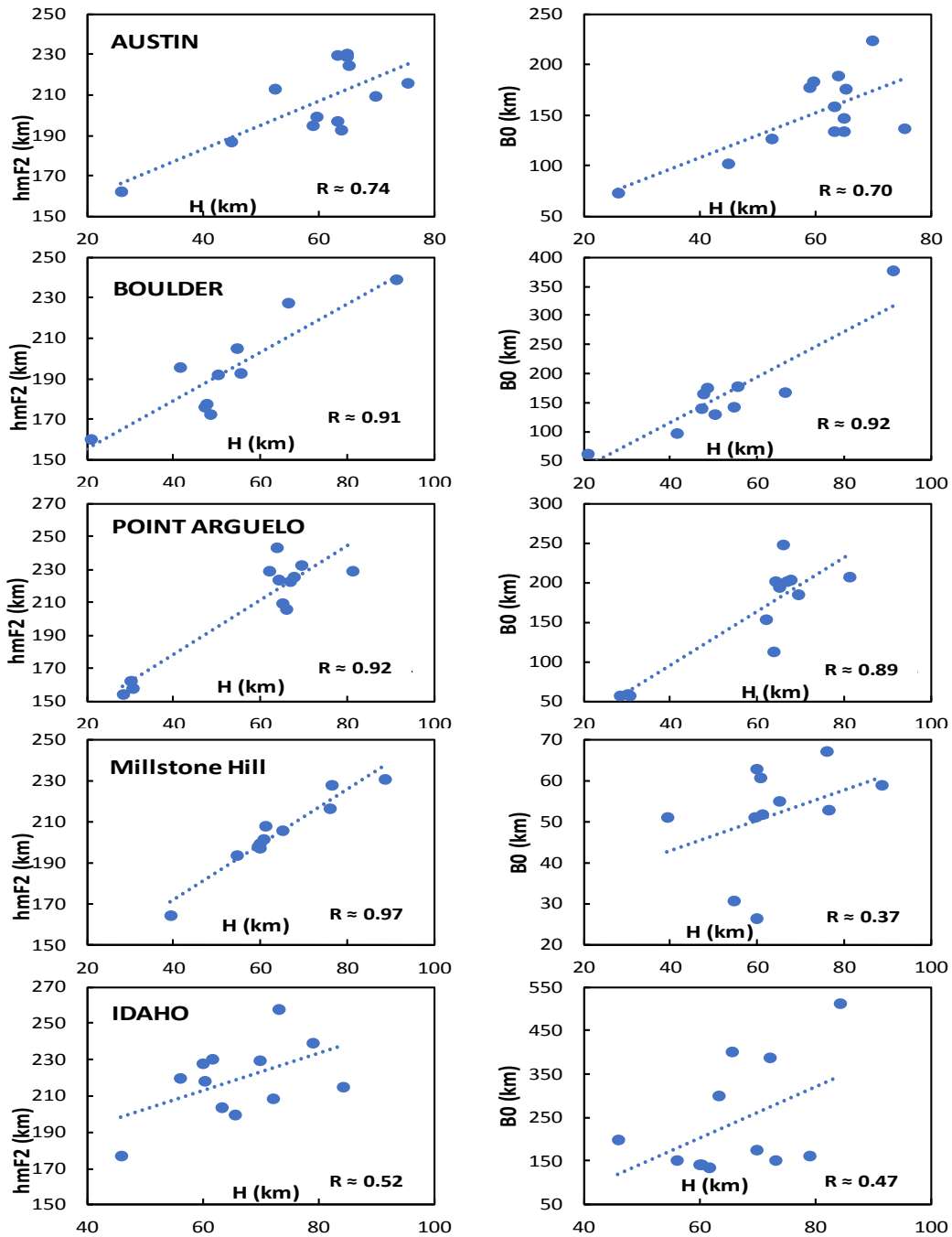
462

463

464

**Figure 3:** Percentage deviation of NmF2 (DNmF2) and hmF2 (DhmF2) magnitudes during the 21 August 2017 eclipse phase.





465

466

467

**Figure 4:** Linear relationship of H versus hmF2 and H versus BO during the eclipse of 21 August 2017 progression phase.